# Lunar surface rock abundance and regolith fines temperatures derived from LRO Diviner Radiometer data

Joshua L. Bandfield,[1] Rebecca R. Ghent,[2] Ashwin R. Vasavada,[3] David A. Paige,[4] Samuel J. Lawrence,[5] and Mark S. Robinson[5]

Received 16 May 2011; revised 21 June 2011; accepted 18 July 2011; published 3 December 2011.

[1] Surface temperatures derived from thermal infrared measurements provide a means of understanding the physical properties of the lunar surface. The contrasting thermophysical properties between rocks and regolith fines cause multiple temperatures to be present within the field of view of nighttime multispectral data returned from the Lunar Reconnaissance Orbiter (LRO) Diviner Radiometer between 60°N/S latitudes. Regolith temperatures are influenced by the presence of rocks in addition to factors such as the thermophysical properties of the regolith fines, latitude and local slopes, and radiative heating from adjacent crater walls. Preliminary comparisons of derived rock concentrations with LRO Camera images show both qualitative and quantitative agreement. Although comparisons of derived rock concentrations with circular polarization ratio radar data sets display general similarities, there are clear differences between the two data sets in the relative magnitude and areal extent of rocky signatures. Several surface units can be distinguished based on their regolith temperature and rock concentration values and distributions including maria and highlands surfaces, rocky impact craters, rilles, and wrinkle ridges, dark mantled deposits, and isolated cold surfaces. Rock concentrations are correlated with crater age and rocks are only preserved on the youngest surfaces or where steep slopes occur and mass wasting prevents mantling with fines. The presence of rocky surfaces excavated by young impacts allows for the estimation of minimum regolith thickness from the size of the impact. The derived rock concentrations confirm the presence of thicker regolith cover in the highlands and in locations of radar-dark haloes.

**Citation:** Bandfield, J. L., R. R. Ghent, A. R. Vasavada, D. A. Paige, S. J. Lawrence, and M. S. Robinson (2011), Lunar surface rock abundance and regolith fines temperatures derived from LRO Diviner Radiometer data, *J. Geophys. Res.*, *116*, E00H02, doi:10.1029/2011JE003866.

## 1. Introduction

[2] The development and reworking of planetary surfaces in a vacuum environment is dominated by impact processes and lack the influence of aeolian and fluvial processes that are prevalent on planets such as Earth and Mars. The surface layer records the history of the interaction between the Moon and the outside environment throughout its history. By understanding this history, we can better understand several basic aspects of lunar science, which is also likely to have direct relevance to the surfaces of other airless bodies within the Solar System. In addition, the lunar surface layer is the principal factor influencing most remote sensing measurements and it is crucial to understand the relationship between the regolith at the lunar surface and the primary igneous materials from which it is derived.

[3] There are few terrestrial analogs that provide a means to determine the connection between the processes unique to the vacuum and space weathering environment and the resulting development of planetary surfaces. We are required to rely on remote observations as well as samples and observations collected at landing sites. The Apollo, Surveyor, and Luna programs provided a great deal of detailed information about the compositional and physical properties of the lunar regolith for a limited number of sites [*Heiken et al.*, 1991]. Remotely sensed observations have extended the coverage across large areas, especially using Earth based observations of the nearside [e.g., *Thompson et al.*, 1974; *Mendell*, 1976; *Helfenstein and Veverka*, 1987; *Ghent et al.*, 2005; *Campbell et al.*, 2007].

[1]Earth and Space Sciences, University of Washington, Seattle, Washington, USA.
[2]Department of Geology, University of Toronto, Toronto, Ontario, Canada.
[3]Jet Propulsion Laboratory, California Institute of Technology, Pasadena, California, USA.
[4]Earth and Space Sciences, University of California, Los Angeles, California, USA.
[5]School of Earth and Space Exploration, Arizona State University, Tempe, Arizona, USA.


0148-0227/11/2011JE003866

[4] Remote observations acquired at ultraviolet through microwave wavelengths have been used to characterize lunar regolith properties. Each style of observation has its own unique set of sensitivities that when used in combination can leverage a more complete characterization of lunar surface properties [e.g., *Thompson et al.*, 1974]. Radar observations, for example, are highly sensitive to the presence of rocks similar in size to the wavelength of measurement. In addition, radar observations have the ability to probe the subsurface and glean information about buried rocks or potential layering. By contrast, reflected light observations at short wavelengths are sensitive to the composition and physical properties of the upper few millimeters of surfaces, which are typically dominated by the regolith fines.

[5] Surface temperatures derived from thermal infrared (TIR) measurements provide a third means of understanding the physical properties of the lunar surface. These measurements are sensitive to the thermal conductivity of the surface layer to a depth that scales with the square root of the time period of the energy input (e.g., the diurnal energy cycle). The lunar diurnal cycle results in depths of sensitivity that vary from several centimeters for highly insulating regolith fines up to meter scales for highly conducting solid rock. The highly contrasting thermal conductivity between lunar rocks and regolith fines results in a large temperature contrast between these materials [*Roelof*, 1968]. Previous work has used these properties to characterize the lunar surface using TIR telescopic measurements as well as the Apollo 17 Infrared Scanning Radiometer and the thermal imager on the Midcourse Science Experiment (MSX) [*Shorthill*, 1970; *Mendell and Low*, 1974; *Price et al.*, 2003].

[6] We continue this work using data returned from the Lunar Reconnaissance Orbiter (LRO) Diviner Radiometer. Specifically, we describe here the influence of rocks on nighttime surface temperatures at low to midlatitudes and separate their effects from regolith fines temperatures. This provides a global characterization of rock distributions on the lunar surface as well as global thermophysical units. A comprehensive study of lunar surface thermophysical properties using Diviner data is beyond the scope of this work, especially with respect to the characterization and thermophysical modeling of the lunar regolith fines.

## 2. Data and Methods

### 2.1. Diviner Instrument and Data Description

[7] The Diviner Radiometer is primarily a thermal infrared radiometer with 7 spectral channels; 3 spectral filters are near 8 $\mu$m wavelengths and separate filters cover ~13–23, 25–41, 50–100, and 100–400 $\mu$m wavelengths [*Paige et al.*, 2010]. Each channel consists of a 1 by 21 element detector array and separate spectral channels are arranged and data are collected in a pushbroom configuration. The spatial sampling of Diviner is ~160 by 320 m from a 50 km polar orbit and the local time of observations migrated across the full diurnal cycle throughout the primary LRO mission. More complete descriptions of the Diviner instrument characteristics and operations are given by *Paige et al.* [2010].

[8] We used data collected from July 5, 2009 through November 30, 2010 for this study. Data were restricted to local times of 1930 to 0530 with solar incidence angles greater than 90 degrees, latitudes between 60°N and 60°S, emission angles less than 15 degrees, and brightness temperatures less than 200 K. The latitude restriction was included because of the large influence of slopes on surface temperatures at higher latitudes that persists throughout the lunar night. Unresolved slopes will contribute to anisothermality that would be incorrectly modeled as increased rock concentrations. Several quality constraints present in the Diviner Reduced Data Records (RDR's) available at the Planetary Data System (PDS) repository were used as well (quality flag for calibration – 0; quality flag for miscellaneous – 0; noise quality flag – 0 to 1).

[9] Only Diviner channels 6, 7, and 8 were used with full width half max (FWHM) band passes of 13–23, 25–41, and 50–100 $\mu$m respectively. The shorter 8 $\mu$m channels 3–5 were not used because they do not have adequate signal-to-noise ratios (SNR) at the relatively cold lunar nighttime temperatures used for this study. At 90 K, the SNR in Diviner channels 3–5 is <1, even when taking into account the fact that most spatial bins include an average of 10s of measurements. Channel 9 (100–400 $\mu$m) was not used because significant drifts in brightness temperature are present in the channel 9 data immediately following calibration observations that would interfere with the analysis if included.

[10] Data from each channel were binned at 32 pixels per degree in ten separate one hour increments of local time from 1930 to 0530. Because of the ground track walk and local time drift of the LRO orbit, most surfaces are covered by only a single acquisition time, but include up to ~10 separate measurements for each channel. In some cases, surfaces are covered by multiple observations acquired ~6 or 12 months apart. Lunar obliquity and variations in solar distance between data acquisition dates may result in different temperatures for a surface at a given local time. However, the resulting differences in nighttime temperatures are small (<0.5 K). A greater variation in temperature between observations that fall within a single 1 h bin can occur due to variations in local time of the observation. For equatorial observations, this can be as much as 7 K for observations collected at the start and end of the 1930–2030 time bin. The resulting data present in the bin will be the average of the separate measurements and local times, and the resulting effect on derived rock abundance and regolith temperatures is negligible.

[11] We included data collected in the pre-mapping 30 × 216 km orbit during the first 60 days after the lunar orbit insertion sequence [*Tooley et al.*, 2010] resulting in variable spatial resolution data. The 32 pixels per degree (PPD) bin size effectively resamples the data to ~500–1000 m/pixel and in most cases spatial resolution is reduced by a factor of 2–4, but with the higher altitude pre-mapping orbit data acquired near periapsis at higher latitudes, data can be oversampled by a factor of ~2 in the cross-track direction.

[12] Data from each spectral channel are acquired separately with no attempt to co-locate separate spectral channels. The resulting data may include observations from separate channel centers up to ~1.4 km apart at opposing corners within a bin. This can result in spurious and nonphysical results in regions of high spatial variability, such as at the edge of a crater rim. In practice, this result was not

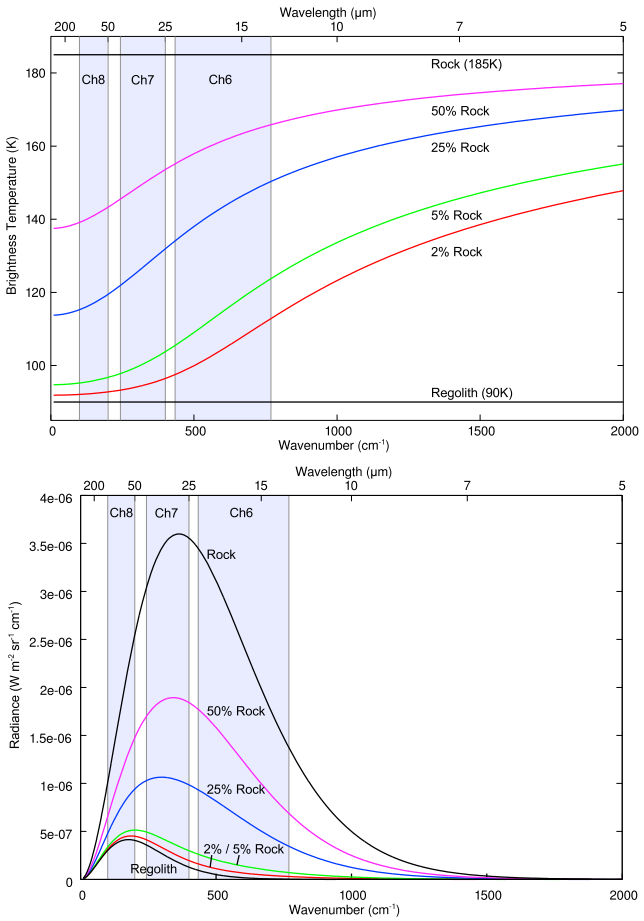


**Figure 1.** (top) Brightness temperature and (bottom) radiance as a function of wavelength for rock/soil mixtures. The wavelength coverage of Diviner spectral channels 6–8 used in this study are shown in light gray. For this simple example, rock is assumed to be at 185 K and regolith is at 90 K with all materials having unit emissivity. Brightness temperatures increase with decreasing wavelength and warmer temperatures have an increased proportional influence on brightness temperature and radiance at shorter wavelengths.

found to be common in the derived rock abundance and regolith temperature data sets.

### 2.2. Methodology

[13] The derivation of rock abundance relies on the presence of multiple temperatures present within the field of view (FOV) of the measurement and the nonlinear nature of Planck radiance with respect to wavelength. Multispectral measurements can be used to estimate the distribution of temperatures present within the measurement FOV. The estimated temperature distributions can be used to derive surface properties such as surface rock fraction or surface slope distributions [*Christensen*, 1986; *Colwell and Jakosky*, 2002; *Nowicki and Christensen*, 2007; *Bandfield and Edwards*, 2008; *Bandfield*, 2009]. This anisothermality that results from the presence of different materials within a particular FOV radiating at different temperatures can be expressed as brightness temperature as a function of wavelength. For example, in the case of an anisothermal surface, the measured brightness temperature approaches the weighted average of those temperatures present with increasing wavelength (Figure 1). The measured brightness temperature approaches the highest temperature present in the scene with decreasing wavelength. As a result, the measured brightness temperature will fall somewhere between the scene average temperature and the highest temperature present regardless of the wavelength of measurement.

[14] It is important to note that a warmer surface does not necessarily result in a higher rock concentration. For example, equator facing slopes will retain higher temperatures throughout the lunar night, but all spectral channels will show equally elevated brightness temperatures. In a similar manner, rille and crater floors may be radiatively heated by nearby walls, but this effect will not increase anisothermality that would lead to an increased rock concentration retrieval.

[15] In practice, data are limited by wavelength range, the number of spectral channels available, instrument precision, and systematic errors. In addition, the relatively subtle variations in the spectral shape of Planck radiance over the temperatures and wavelengths measured do not allow for the unique identification and separation of more than a few temperatures. Our implementation of rock abundance and regolith fines temperature retrieval uses the binned Diviner channel 6–8 radiance described above. These three measurements are fit in a least squares manner using a simple model with two parameters; 1) rock areal fraction (0–100%), and 2) regolith fines temperature.

[16] Rock temperatures are modeled a priori using the properties for vesicular basalt described by *Horai and Simmons* [1972] and the 1-dimensional thermal model described by *Vasavada et al.* [1999]. We used a density of 2940 kg/m$^3$, thermal conductivity of 1.491 W/(m K), and a temperature dependent heat capacity of $(-154.9 + 4.983 \cdot T - 0.008207 \cdot T^2 + 0.000005192 \cdot T^3)$ J/(kg K), where T is temperature in K [*Horai and Simmons*, 1972]. Although the temperature dependence of thermal conductivity may be significant for regolith fines in a vacuum environment, it is not significant for solid materials. Using these parameters, our thermophysical definition of a rock has a thermal inertia of 1570 $J \cdot m^{-2} \cdot K^{-1} \cdot s^{-1/2}$ at 200 K. Rock temperatures were modeled assuming an albedo of 0.15 and emissivity of 0.95 and an infinitely thick, level, and laterally continuous layer. The albedo chosen was a moderate value in between that of highlands and maria. The temperature effects due to variations in albedo are largely dissipated during the lunar night and are less than ±1 K. Temperatures were modeled at equinox and seasonal variations in temperature were not taken into account. As discussed above, seasonal effects do not result in significant changes in surface temperatures in nighttime data at low and midlatitudes. A rock temperature lookup table was constructed at 5 degree latitude and 15 min local time intervals over the course of the lunar day. Modeled temperatures at the equator range from 238 to 203 K at a local time of 1930 and 0530 respectively. At 60°N, modeled temperatures are 212 to 185 K for the same local times of 1930 and 0530. The rock temperatures used in the fitting of the Diviner data are linearly interpolated using this lookup table for each latitude and local time.

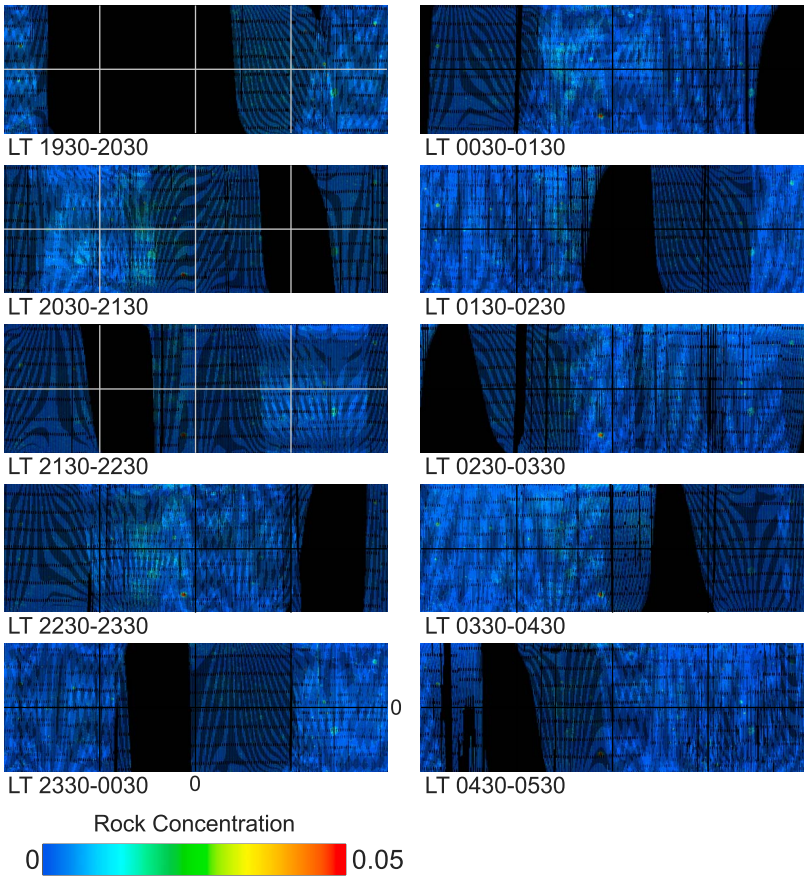


**Figure 2.** Rock concentration maps derived from local times of 1930 through 0530. The maps cover all longitudes and 60°N to 60°S with the equator and prime meridian at the center of each image.

[17] The modeled Diviner channel 6–8 radiance is produced using the predicted rock temperature and an initial guess for the rock areal fraction and regolith temperature. Temperatures are converted to radiance using a lookup table of Planck radiance convolved with the Diviner instrument response functions for each channel. The radiances for rock and regolith temperatures are added together weighted by the rock areal fraction. For each latitude/longitude/local time bin, the root mean squared (RMS) difference between modeled and measured radiance is calculated. In this manner, the RMS difference is minimized using the optimal combination of regolith temperature and rock areal fraction. The minimization routine is well-behaved and predictable. Convergence on optimal values is rapid and assumes RMS differences are a quadratic function of the individual variables to select predicted minimum values for the subsequent iteration. Rock fractions are forced to be greater than or equal to zero.

[18] This methodology relies on several simplifying assumptions. The primary motivation for these assumptions is the relatively simple nature of the data (3 values of radiance) that precludes the retrieval of information from a more complicated model. For example, we attempted to solve for rock temperatures in addition to regolith temperature and rock areal fraction. Although three measurements and three unknowns are present, the solution is non-unique and convergence on a solution is highly unstable. There is ambiguity inherent in the problem because a surface composed entirely of rocks can either lead to a solution of 100% rocks with any regolith temperature (since regolith does not contribute to the solution in this case) or 0% rocks and a regolith temperature that is the same as that predicted for rocks.

[19] What qualifies as a "rock" according to the modeling here is dependent on both the size of the object and the time at which it is observed. Using the range of values for basaltic rock and breccia density, heat capacity, and thermal conductivity, the skin depth of rock under lunar diurnal conditions is ~0.5–1 m for a horizontally continuous slab. In reality, rocks are not continuous slabs, but are protruding, partially buried, subject to differential heating as a function of latitude and time of day, and mantled with regolith fines [*Roelof*, 1968]. In addition, smaller rocks cool faster over the course of the night than large rocks, so that they are at temperatures similar to larger rocks early in the night, but approach the temperature of the colder regolith fines near sunrise. Other situations may be present as well, such as radiative and conductive warming of regolith surfaces by adjacent rocks. There are many complicating "real world" factors that are not modeled here. We have taken a pragmatic approach to assessing the potential errors in the retrieval algorithm and have compared our results with

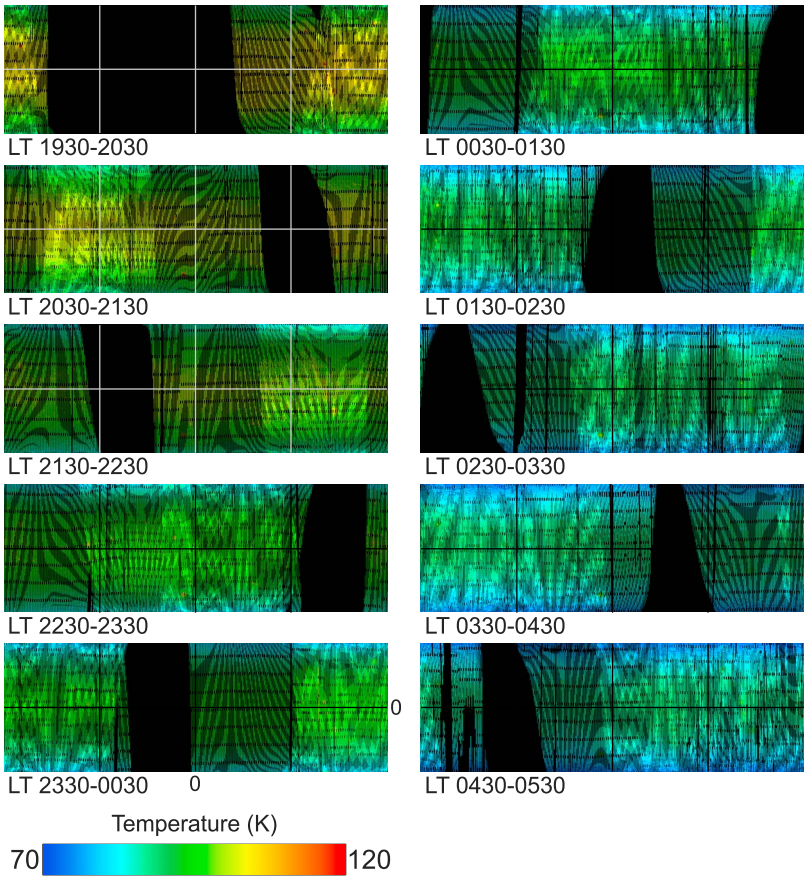


**Figure 3.** Rock-free regolith temperature maps derived from local times of 1930 through 0530. The maps cover all longitudes and 60°N to 60°S with the equator and prime meridian at the center of each image. The temperature dependence on both latitude and local time is clearly apparent in the images.

high-resolution Lunar Reconnaissance Orbiter Camera (LROC) [*Robinson et al.*, 2010] images.

[20] To provide a sense of the precision of the algorithm, we used synthetic radiance constructed assuming a regolith temperature of 93 K and a 1% rock concentration at 204 K (temperature values are for a local time of 0500 at the equator). Random noise (as documented for Diviner channels 6–8 [*Paige et al.*, 2010]) was added to a set of 10000 spectra. Rock concentration and regolith temperature values were retrieved using the algorithm described here. Average retrieved regolith temperatures were 92.9 K with a standard deviation of 0.94 K. Average retrieved rock concentration values were 0.010 with a standard deviation of 0.0015. The derived rock concentration and regolith temperature values are stable at the noise equivalent radiance levels of Diviner.

[21] In addition, it is possible to instead solve for rock temperature and areal fractions using assumed regolith temperatures. However, most surfaces have rock coverage close to zero and even surfaces considered "rocky" typically have fractions less than 10%. Uncertainties in rock temperatures result in abundance uncertainties that are roughly proportional to the rock areal fraction. A 5 K error in regolith fines temperature for a surface composed of 99% regolith will result in much larger retrieval errors than the same 5 K error in the assumed temperatures of rocks covering 1% of the surface.

## 3. Results

### 3.1. Global Maps

[22] 89.5 million separate rock concentration and regolith temperature retrievals were calculated from the global binned Diviner channel 6–8 radiance data set (Figures 2–4). Ten separate maps were produced for each 1 h bin of local time and surface coverage is 89.8%, accounting for the variable coverage of the spatial bins as a function of latitude. Average RMS error between measured and modeled spectra is 0.0079 W $cm^{-2}$ $\mu m^{-1}$ (2.5% of the measured radiance) corresponding to a difference in brightness temperature of 0.9, 0.4, and 1.1 K for Channels 6–8 at 90 K respectively. There is no distinct trend in RMS error with rock concentration and a slight correlation with regolith temperature (Figure 5).

[23] Global average rock concentration within the ±60° latitude range is 0.004. Small, but systematic differences in rock concentrations are present between different local times, ranging from an average of 0.003 to 0.005. Although some of this difference can be attributed to different geographical coverage between the separate local time maps,

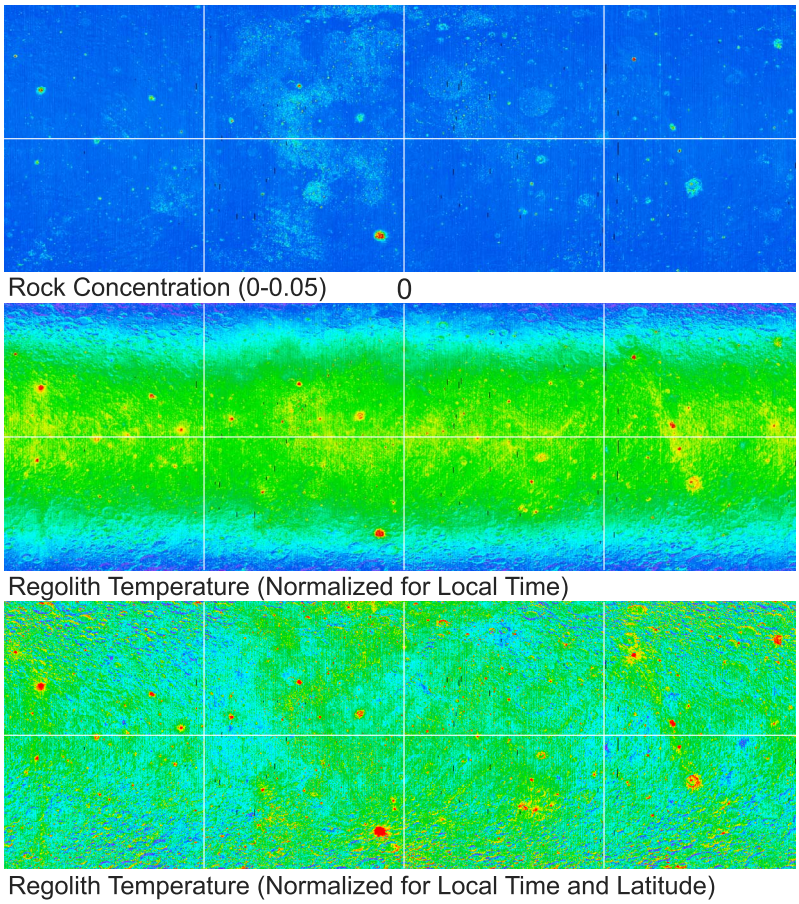


**Figure 4.** (top) Rock concentration and (middle and bottom) regolith temperature maps. All maps cover all longitudes and 60°N to 60°S and are resampled to 4 pixels per degree. The rock concentration map is the average of the 10 maps shown in Figure 2 with the same color scale. The rock-free regolith temperature maps were composed by individually stretching the 10 local time images shown in Figure 3. In addition the latitudinal gradient was removed from the bottom regolith temperature map to enhance local variations. The large variations in regolith temperature due to latitude and local slopes are well-separated and not apparent in the rock concentration map.

the differences persist when comparing only coincident pixels. 99.995% of measured surfaces have rock concentrations less than 0.20 and no pixels show rock fractions above 0.70. Where low rock concentrations are present, there is a clear decrease in retrieved rock concentration throughout the lunar night (Figure 6) and rock concentrations retrieved from observations acquired at local times between 0430 and 0530 are only about 65% of those acquired between 1930 and 2030. Distinct trends in average rock concentration as a function of latitude are also present in early evening retrievals, but are largely absent from predawn measurements (Figure 7). There is no distinct latitudinal trend present for surfaces with elevated rock fractions.

[24] Derived regolith temperatures have clear trends with latitude and local time, as expected (Figure 8). Global average regolith temperatures decrease from 103.6 K between 1930 and 2030 to 90.1 K between 0430 and 0530. Post-sunset (1930–2030) temperatures decrease from ~108 K to 95 K between 0° and 60°N/S latitude, respectively. Predawn (0430–0530) temperatures decrease from ~94 K to 83 K between 0° and 60°N/S latitude, respectively.

[25] Regolith temperatures and rock concentrations are highly correlated within local regions. For example, craters that display elevated rock concentrations also display elevated regolith temperatures. However, distinct differences are present in the spatial distribution of elevated rock concentrations and regolith temperatures. In many cases, elevated regolith temperatures are present over the ejecta, rims, walls, and floors of craters, whereas elevated rock concentrations are often absent from crater floors and distal ejecta. Rock concentrations and regolith temperatures are not coupled at the global level and regolith temperatures have a strong dependence on latitude, local time, and local slopes. Regolith temperatures over rock-free regions show a range of ~40–110 K, indicating that isothermal and anisothermal variations are cleanly separated by the Diviner multispectral data.

### 3.2. Surface Units

[26] Several surface units can be distinguished based on their regolith temperature and rock concentration values and distributions as well as morphological characteristics (Figure 4). These units include typical maria and highlands

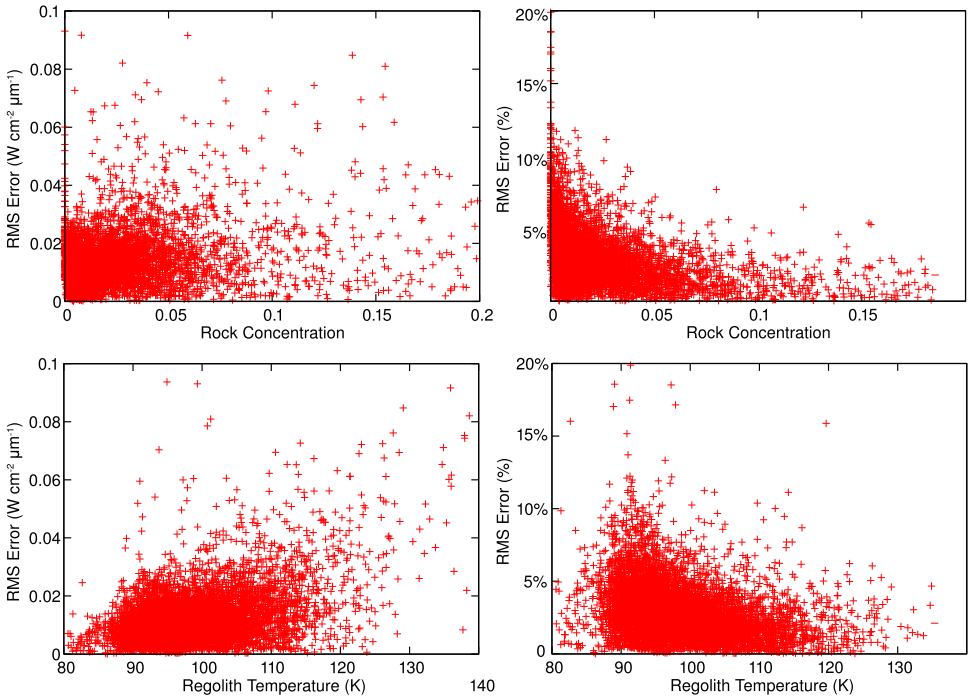


**Figure 5.** RMS fitting error versus (top) rock concentration and (bottom) regolith temperature. Data include every 10th point taken from 345 to 353°E, 40–46°S covering Tycho Crater and the surrounding area. There is no apparent correlation between rock abundance and RMS error, but higher regolith temperatures do tend to have slightly higher RMS errors.

surfaces, rocky young impact craters, rilles, and wrinkle ridges, dark mantled deposits, and isolated cold surfaces.

[27] Maria plains surfaces typically have low rock concentration values (typically <0.5%), but numerous small craters (>100s of m in diameter) expose abundant rocks. In many cases, these craters cannot be resolved at the resolution of the maps produced here, but their contribution to the overall signal is strong enough to significantly raise the rock concentration of the pixel. Regolith temperatures follow a trend typical of most highlands and mare surfaces. However, the numerous small rocky craters also produce elevated regolith temperatures correlated with the elevated rock concentrations.

[28] Highlands surfaces are also characterized by low rock concentration values; however, in contrast to the maria, craters do not typically expose rocky surfaces. Within these regions, only larger (>5–10 km) relatively fresh craters have elevated rock concentrations. Regolith temperatures are similar to those of most highlands and mare surfaces. However, the presence of numerous slopes causes more variability in regolith temperatures within the rough high-

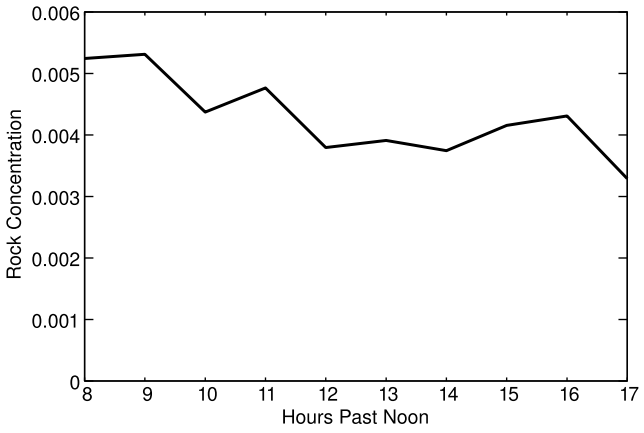


**Figure 6.** Global average rock concentration values for each of the 10 local times shown in Figure 2. There is a distinct decreasing trend in derived rock concentrations through the lunar night.

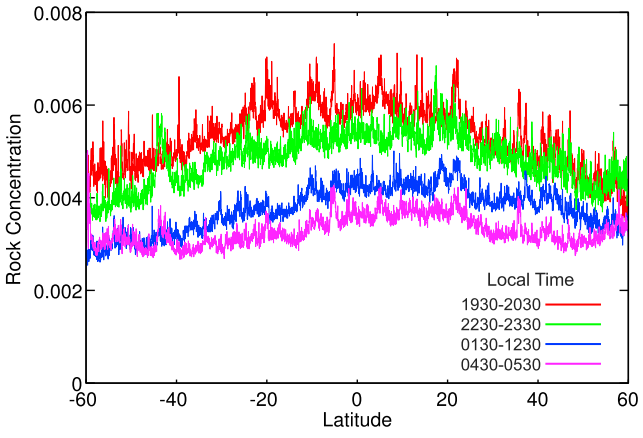


**Figure 7.** Longitudinally averaged rock concentration values for 4 separate local time bins. There are clear trends in rock concentration as a function of latitude and local time present, though some of the latitudinal dependence is correlated with the location of maria.

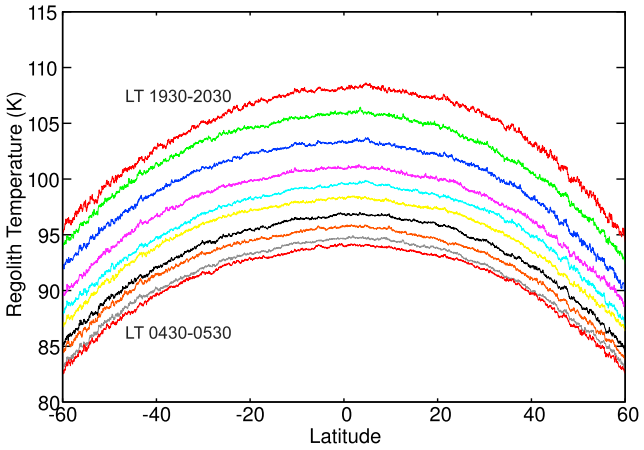


**Figure 8.** Longitudinally averaged regolith temperature values for each of the 10 local times shown in Figure 3. The nighttime cooling trend is apparent with each succeeding local time.

lands surfaces, especially at higher latitudes. As with the maria surfaces, regolith temperatures are higher where rock concentrations are elevated.

[29] Dark mantled deposits are characterized by smooth, relatively low-albedo surfaces and are hypothesized to be pyroclastic in origin [e.g., *Gaddis et al.*, 1985]. These surfaces are characterized by uniformly low rock concentrations and regolith temperatures such as can be seen on the Aristarchus Plateau or Rimae Bode. Where craters are present, they do not typically expose rocks or show elevated regolith temperatures.

[30] Relatively fresh craters expose areas of elevated rock concentrations and high regolith temperatures. Large craters, such as Tycho, have extensive rocky and relatively warm regolith surfaces that cover the floor, walls, rim, and ejecta within 1 crater radius. The regions of elevated rock concentrations and high regolith temperatures are nearly coincident. This correlation often breaks down for smaller craters (<15 km in diameter). In some cases, the crater floors are relatively rock-free, but have high regolith temperatures. In other cases, small (<5 km in diameter) young craters have rocky ejecta extending ~1–1.5 crater radii from the crater rim, but with high regolith temperatures extending up to 3–4 crater radii from the crater rim. Although not always the case, smaller, fresh craters often have more extensive areas of high regolith temperatures relative to areas of elevated rock concentrations.

[31] Exposures of elevated rock concentrations are typically associated with craters, rilles and wrinkle ridges and other surfaces where steep slopes are present. As with the smaller craters, regions of high regolith temperatures appear more extensive than regions of elevated rock concentrations.

[32] An additional anomalously rocky region is located near 168°E, 42°N, covering an area approximately 100 km in diameter. Areas of elevated rock concentration are nearly coincident with areas of high regolith temperatures. Although the surface is rough and contains numerous craters, the surfaces with elevated rock concentrations are patchy and not obviously associated with the craters. This region is otherwise nondescript and is apparently unique with regards to these properties.

[33] Numerous isolated locations within the maria and highlands contain anomalous regolith temperatures that are commonly 5–10 K colder than the surrounding rock-free regolith surfaces throughout the lunar night. These low regolith temperatures are typically associated with a fresh, rocky crater at the center of the cold region. Rock concentrations are uniformly low within these cold areas

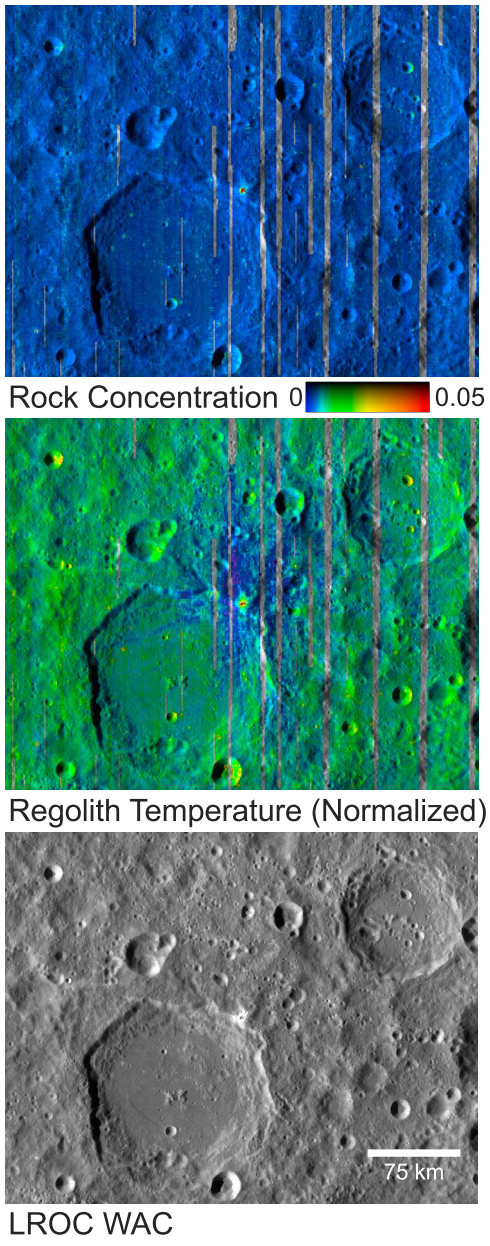


**Figure 9.** Example region containing anomalously cold regolith temperatures centered near 151.7°E, 4.1°S. (top) Rock abundance shows no variation except within the immediate vicinity of the crater. (middle) Low regolith temperatures extend up to ~100 km from the crater in distinct rays. (bottom) There is no associated albedo or morphological signature present in LROC wide-angle camera data or other low spatial resolution imaging data sets.

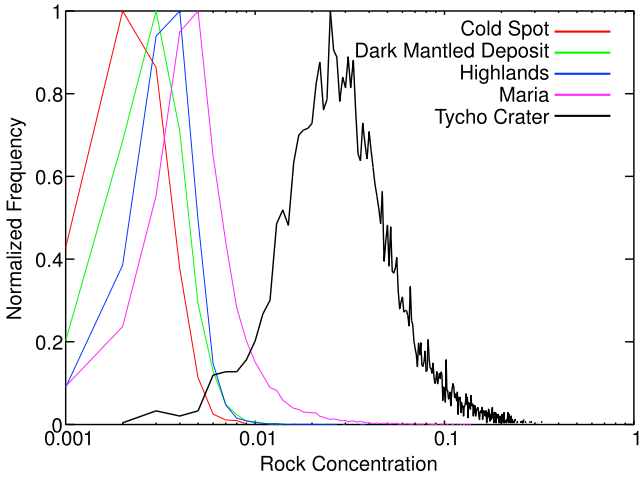


**Figure 10.** Distribution of rock concentration values over representative surface thermophysical units. Data are binned in increments of 0.001 (0.1%) and normalized to the peak bin value. Small rocky craters contribute to the long tail of high rock concentration values in the maria. Tycho Crater is a particularly rocky region, but is still dominated by surfaces with <10% rock coverage.

(<0.3%). The largest of these regions covers a region ~100 km in diameter with a 1.5 km diameter crater at the center near 151.7°E, 4.1°S (Figure 9). Rays or streamers of the "cold spots" are apparent up to ~200 km from the center, but are typically <15 km in diameter. There is no apparent visible/near-infrared color or albedo difference associated with these low temperature surfaces.

[34] Because of latitude differences in the coverage of the various surface units, it is not possible to directly compare their regolith temperatures. However, we can compare the rock concentration values and we find that they do not display a significant dependence on latitude (except where maria surfaces are also correlated with equatorial and low northern latitudes; Figure 10). Modal rock concentrations increase slightly from the cold spots to dark mantled deposits, highlands, and maria (from 0.2 to 0.5%). Only maria, fresh craters, and the anomalously rocky region discussed above have a significant fraction of their surfaces with elevated rock concentrations. The example cold spots, dark mantled deposit, highlands, maria, anomalously rocky, and young crater surfaces presented here have 0.1, 0.4, 0.5, 18.6, 63.5, and 98.4%, respectively of their surfaces with >1% rock concentrations.

### 3.3. Validation and Comparison With the Imaging and Radar Data Sets

[35] We completed a preliminary assessment and comparison of rock abundance with the LRO Camera (LROC). LROC is typically sampled at 0.5 or 1.0 m/pixel, which allows for resolution of objects 1.0 or 2.0 m across, respectively. In practice, only blocks larger than ~2 m could be unambiguously identified and it is likely that some blocks <3 m in diameter would escape detection.

[36] A quantitative comparison was done using a 0.4 by 2.0 km subset of LROC image M121423567R, located within the central peak of King Crater near 120.66 E, 5.06 N (Figure 11). This region covers half of two Diviner rock concentration bins with 10.0 and 10.6% rock concentration values. Only rocks that could be unambiguously identified as such were counted. In each case, 3 points were selected on the edge of each rock that defined a circle that was used to determine diameter and area. A total of 769 blocks were identified over an area of 0.848 km2 and were placed into 1 m diameter bins (Table 1).

[37] Block counts increase with decreasing diameter, but decrease in number at the 2–3 m bin and no blocks <2 m in diameter were confidently identified. This pattern is due to the functional limit of the spatial resolution and it is probable that any block counts for sizes <3 m in diameter are under-counted. Given the expectation of increasing numbers of rocks with decreasing diameter and the sensitivity of Diviner data to rocks ~1 m in diameter, the LROC block counts are likely to be a significant underestimate. This is also suggested by comparison with Diviner rock concentration values as the direct counted areal fraction of the comparison area is 1.5%, significantly less than the 10.3% estimation from Diviner. However, assuming an accurate block count at >3 m in diameter, the lunar cumulative block size distribution can be well represented using a power function [*Cintala and McBride*, 1995] (Figure 12). The cumulative rock concentration can be represented by the function $c = 0.082\ d^{-1.326}$, where d is the rock diameter and c is the concentration of rocks present with diameters equal to or larger than d. The LROC block counts are well-fit using this relationship with a correlation coefficient of 0.997. For blocks greater than or equal to 1 m in diameter, this relationship predicts a block concentration of 8.2%, in good agreement with the Diviner derived rock concentrations.

[38] This comparison is preliminary and more extensive comparisons are necessary to fully validate and quantitatively compare block concentrations in Diviner and LROC data. It is apparent, however, that at least on a qualitative level, the two data sets are in good agreement with each other. An example is demonstrated in the region of Rima Bode. A rille is present near 356 E, 13 N and rocks are clearly visible and concentrated on the steeper slopes. There is good qualitative agreement between the relative abun-

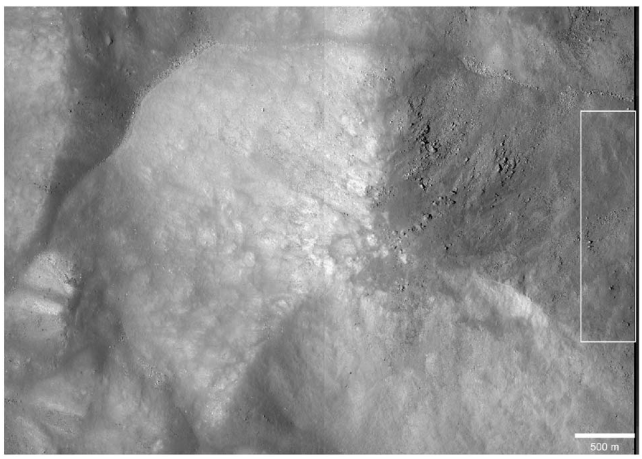


**Figure 11.** Portions of LROC images M121423567L/R covering the central peak of King Crater. A manual rock count was completed within the area denoted by the white box on the right hand side of the image.

**Table 1.** LROC Block Count Results From a Portion of Image M121423567R

| Block Size (m) | Number of Blocks | Blocks/ km$^2$ | Areal Fraction | Cumulative Fraction |
|---|---|---|---|---|
| >11 | 11 | 13.0 | 0.0023 | 0.0023 |
| 10–11 | 12 | 14.2 | 0.0012 | 0.0035 |
| 9–10 | 8 | 9.4 | 0.0007 | 0.0042 |
| 8–9 | 6 | 7.1 | 0.0004 | 0.0046 |
| 7–8 | 23 | 27.1 | 0.0012 | 0.0058 |
| 6–7 | 19 | 22.4 | 0.0007 | 0.0066 |
| 5–6 | 61 | 72.0 | 0.0017 | 0.0083 |
| 4–5 | 177 | 208.8 | 0.0033 | 0.0116 |
| 3–4 | 332 | 391.7 | 0.0038 | 0.0154 |
| 2–3 | 120 | 141.6 | 0.0007 | 0.0161 |
| 1–2 | 0 | 0 | 0 | |
| 0–1 | 0 | 0 | 0 | |

dance of rocks visible in the LROC images and the Diviner rock concentration values. This qualitative agreement appears to be valid for rock concentration values from less than 1% to greater than 10% (Figure 13).

[39] Direct comparison of the Diviner rock concentrations with radar data sets is also possible. The Miniature Radio Frequency (MiniRF) system is a synthetic aperture radar utilizing X-band and S-band frequencies (~3 and 10 cm respectively) at 30 and 150 m sampling [*Nozette et al.*, 2010]. We used the S-band circular polarization ratio (CPR) map-projected level 2 products available at the Planetary Data System (PDS). All data used here were acquired prior to September 19, 2010. The CPR is a dimensionless parameter that is the ratio of the same sense circular polarization return to the opposite sense circular polarization return. This parameter is highly sensitive to scatterers (such as rocks) of roughly the same size as the wavelength of the signal [e.g., *Campbell et al.*, 2010]. In addition, we used the 70 cm Arecibo-based CPR maps (also available at the PDS) for comparison [*Campbell et al.*, 2007]. The MiniRF data were used to illustrate high-resolution details within the Copernicus Crater region and the Arecibo radar data provided a regional synoptic view covering much of Oceanus Procellarum.

[40] Both radar data sets were only used in a qualitative sense. Individual MiniRF images are typically thin strips with high aspect ratios and it is necessary to mosaic the data to produce images that cover larger areas. In order to do this, we removed cross-track gradients from individual MiniRF strips. The resulting data was adjusted using a standard deviation linear stretch and blended where separate observations overlapped spatially to produce seam-free mosaics.

## 4. Discussion

### 4.1. Overview

[41] We have produced quantitative maps of rock concentrations and regolith temperatures. However, even though the results can be described as quantitative, how these numbers relate to actual surface properties is not well defined. Interpretation of these results requires an understanding of the fundamental limitations of the method. The availability of only 3 independent radiance measurements prevents the retrieval of more than a few parameters and the model has been kept necessarily simple. As mentioned above, there are many potential complexities that are not taken into account by this model and all of these factors (and likely many others) add uncertainty to the interpretation of rock concentration and regolith temperature values presented here.

[42] In general, as is well known already, most lunar surfaces are relatively free of rocks. Micrometeorite bombardment and space weathering are the dominant current geologic processes for most lunar surfaces. Rocks are only exposed where mass wasting on steep slopes or recent larger impacts expose larger clasts that have not been exposed long enough to be broken down. The Diviner measurements have provided systematic coverage of the planet with multispectral observations that allow for the separation of the properties of finer materials from those of exposed rocks.

[43] Most surfaces have rock concentrations between 0 and 0.01 and fine distinctions at the 0.001 level can be made between surface units (Figure 10). It is not clear how accurate these small concentrations are, however and other systematic differences are present as illustrated by the variation in rock concentrations with local time (Figure 7). Some of this difference can be attributed to increased sensitivity to smaller rocks early in the lunar night. Residual anisothermality due to surface roughness that persists into the lunar night is not likely a factor as its effects are more pronounced and would lead to higher rock concentrations at higher latitudes, which is not observed. Regardless, given the systematic variability in rock concentrations with local time, small differences (<0.005) do not necessarily reflect actual differences in the abundance of rocks on the lunar surface. However, small relative variations in rock concentrations within similar latitudes and local times are probably valid, consistent with the standard deviation of 0.0015 in rock concentration derived from the sensitivity study discussed above.

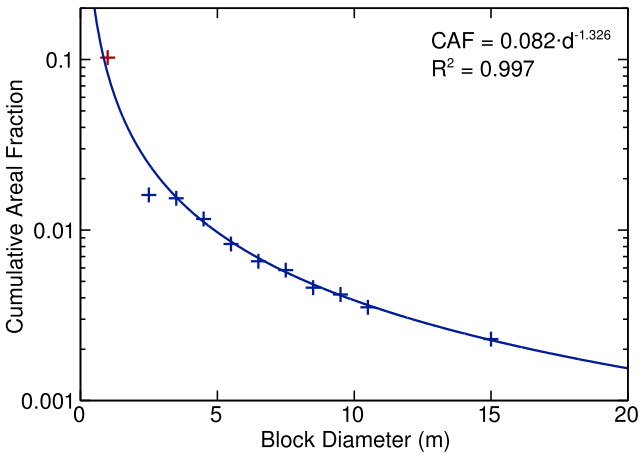


**Figure 12.** Rock count results from the area shown in Figure 9. The blue crosses are the direct calculation of areal coverage of rocks at or larger than the block diameter from the LROC image. The plotted line is the power function regression fit to bins greater than or equal to 3–4 m in diameter. The best fit equation and correlation coefficient are shown in the upper right and the Diviner derived rock concentration value is shown as a red cross.

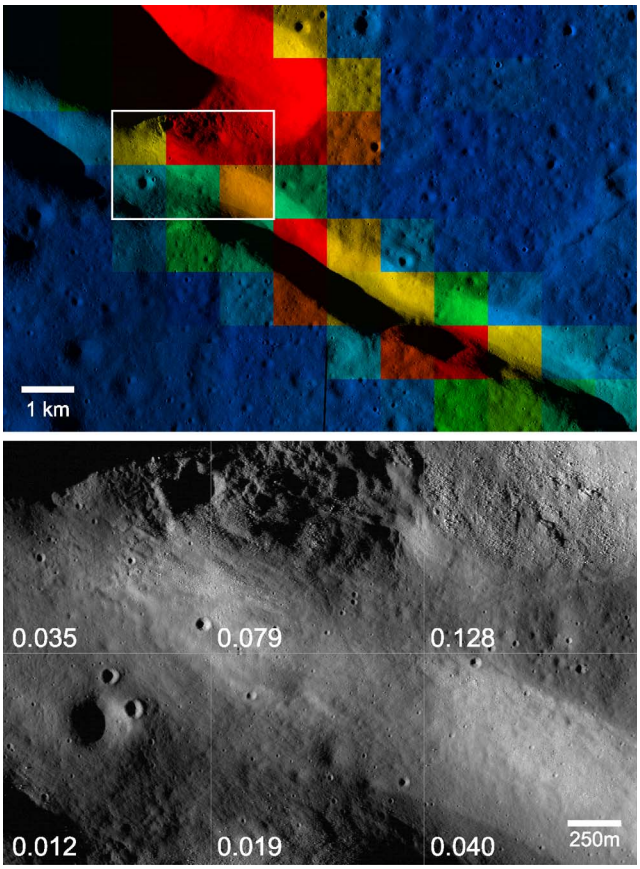


**Figure 13.** (top) Rock concentration values near Rima Bode (356.1°E, 12.9°N) with LROC images M102193170L/R used for shading. The white box denotes the area shown in the bottom image. (bottom) A portion of LROC image M102193170L. Each square in the image covers a separate Diviner bin with the derived rock concentration value listed. There is qualitative agreement between the abundance of blocks apparent in the image and the Diviner derived rock concentration values.

### 4.2. Comparison With LROC Images

[44] Despite this complexity, the results appear to be well-correlated, at least qualitatively, with boulder concentrations directly observable in LROC images. As with the Diviner data products, LROC images have limitations, primarily due to the limit of the image resolution. Fortunately, LROC allows for the identification of boulders of similar scale at which Diviner is likely to be sensitive (~1 m). As shown in Figure 13 and is apparent in many other locations, there is good agreement on a qualitative level between the relative abundance of blocks visible in LROC images and the Diviner derived rock concentration values. Although we have not performed an exhaustive survey, no instances have been identified where there is apparent disagreement between images and rock concentrations. In this sense, the Diviner derived rock concentration maps are accurate. Errors due to misregistration between bands or incorrectly predicted rock temperatures do not appear to significantly affect the qualitative results. It should also be noted that while radiative heating from adjacent surfaces on slopes may result in higher nighttime temperatures, this heating does not have a large effect on the anisothermality. Because the algorithm used for the derivation of rock concentrations is sensitive to increased anisothermality rather than a simple increase in brightness temperature, the derived increase in rock concentrations within depressions such as rilles or craters is not affected by radiative heating effects from adjacent surfaces.

[45] Although only a single region was investigated, rock counts provide a basis for the comparison of image and thermal data sets. The decrease in the number of blocks identified below 3 m in diameter provides a practical sense of the limitations of the LROC data set, even with 0.5 m/pixel sampling. In the example described above, the scaling relationship between cumulative rock areal coverage and minimum block diameter is closely described using a simple power law relationship. The close agreement between the predicted >1 m block diameter areal coverage (8.2%) and the Diviner derived rock concentration value (10.3%) provides limited support that the technique is indeed sensitive to blocks of diameters ~1 m and larger.

[46] Extrapolating the predicted coverage to smaller block diameters illustrates how much rock coverage is likely to be present. For example, 20.5% and 69.2% areal coverages are predicted for block diameters greater than 0.5 and 0.2 m,

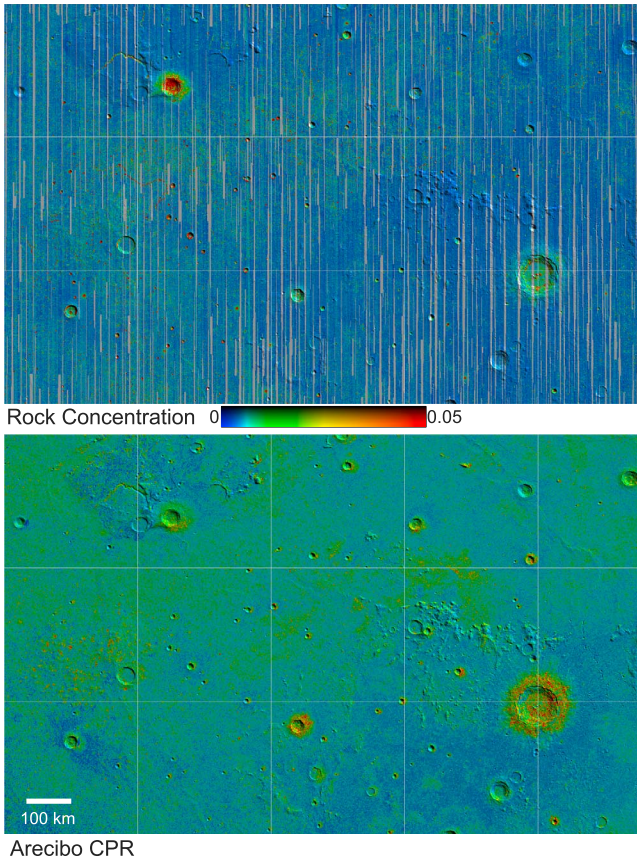


**Figure 14.** (top) Rock concentration and (bottom) Arecibo 70 cm circular polarization ratio (CPR) [*Campbell et al.*, 2007] maps. The images cover 300–350°E and 0–30°N and Lunar Orbiter Laser Altimeter (LOLA) data are used for shading. Regions of high CPR are interpreted as having higher abundances of blocks within ~10 m of the surface.

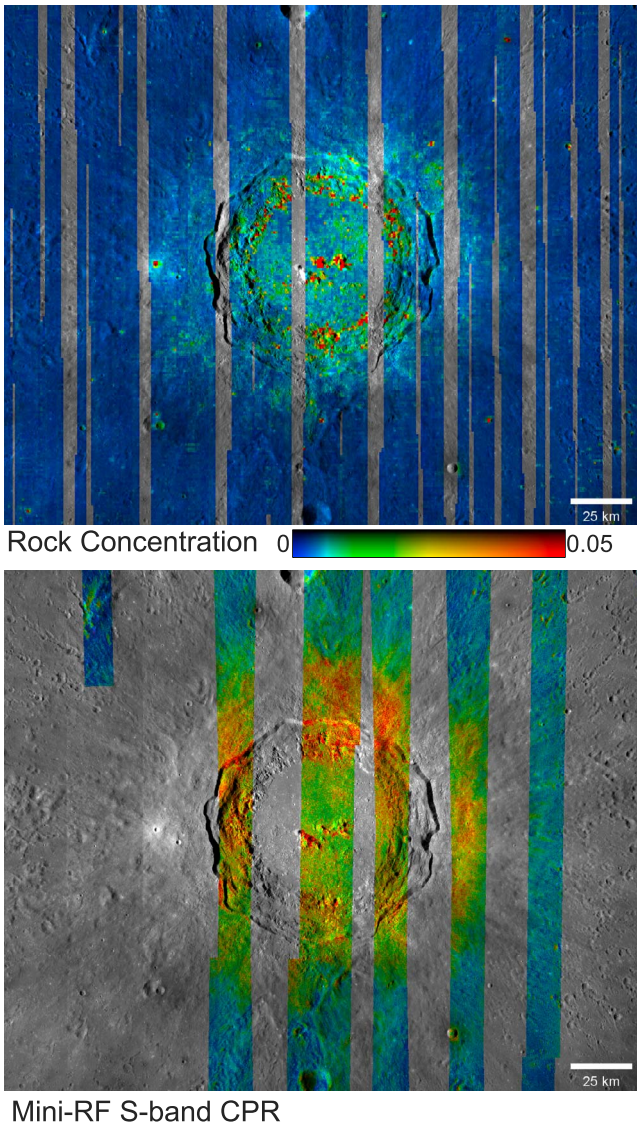


**Figure 15.** Rock concentration (top) and MiniRF S-band circular polarization ratio (CPR) image mosaic (bottom) of Copernicus Crater (centered near 339.9°E, 9.6°N). The LROC Wide-angle Camera (WAC) global mosaic is used for shading. Regions of high CPR values extend farther outside the crater rim than elevated rock concentration values.

respectively for the King Crater central peak region discussed here. Despite such large proportions of the surface predicted to be covered by blocks, the 10.3% coverage predicted from the Diviner data set indicates the insensitivity to these smaller block sizes. However, regolith temperatures are also elevated relative to adjacent block-free surfaces. It is likely that the presence of smaller blocks are responsible for these elevated temperatures. In this manner, larger blocks primarily affect the Diviner rock concentration values and smaller blocks likely have a more pronounced effect on the derived regolith temperatures.

### 4.3. Comparisons With Radar Data Sets

[47] There is a general correlation between both radar data sets and the rock concentration maps as would be expected because the radar data sets are highly sensitive to the presence of rocks. Craters (such as Aristarchus, Kepler, Reiner, and Copernicus craters) that show elevated rock concentrations also have high values of CPR (Figures 14 and 15). Where maria surfaces show rocky small craters, the radar data also show increased values of CPR. Other regions, such as Aristarchus Plateau, have low concentrations of rocks and low values of CPR. In a general sense, both data sets are in agreement and clearly distinguish rocky and rock-free regions.

[48] On closer inspection, significant differences in the spatial patterns between the radar and rock concentration data sets are clearly present. For example, the overall rock concentrations in the Aristarchus crater region are significantly higher than the concentrations present in the Copernicus crater region. By contrast, CPR values are clearly lower over Aristarchus than Copernicus. At the basic level, the radar data could be used to interpret Copernicus crater as rockier than Aristarchus crater and the opposite interpretation would be made from the thermal data set. Rocky craters also display distinctly elevated CPR values within ~1 crater radius outside the rim whereas Diviner derived rock concentration values are only slightly elevated and are typically <1%.

[49] These differences are likely due to the depth of sensitivity of the two methods. For dry lunar materials, radar can penetrate to depths of roughly 10 times the wavelength of the measurement [*Campbell et al.*, 1997]; ~1 and 7 m for the MiniRF S-band and Arecibo 70 cm data sets, respectively. By contrast, the Diviner data are primarily influenced by rocks present at the surface. In all but the most recently formed craters, rocks at the surface will be broken down by micrometeorite bombardment in the vacuum environment. However, even shallowly buried rocks will be preserved and detected by the radar while remaining undetected in the thermal data. This difference in sensitivity shows that blocks from crater ejecta and on crater floors are largely buried and not commonly present at the surface.

[50] Many lunar craters are surrounded by a region of low CPR values (referred to as "radar dark haloes"), which have been hypothesized as being a mantle of relatively rock free ejecta [*Ghent et al.*, 2005; *Ghent et al.*, 2008]. Similar spatial patterns are present in the rock concentration data. Although the thermal data are only sensitive to the near-surface materials, relatively young craters of various sizes can be used to probe the nature of the subsurface materials. These craters can expose rocky materials that would otherwise remain buried and undetected in the thermal infrared data.

[51] Smaller craters lack significant rock concentrations in the radar dark halo regions, consistent with previous results that indicate these are thick and relatively rock-free layers of ejecta. Immediately outside the radar dark halo regions within the maria, small craters do commonly have elevated rock abundances indicating that the rock-free regolith is significantly thinner in these regions.

[52] In addition, cold spots do not appear in either the Arecibo or MiniRF data. This may indicate that they are a relatively thin, near-surface phenomenon. By contrast, dark mantled deposits such as Aristarchus Plateau show both uniformly low CPR and rock concentration values. This is consistent with these deposits being relatively thick.

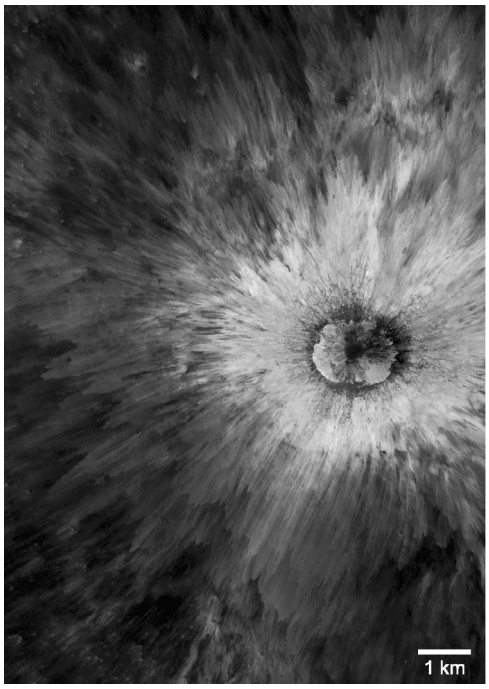


**Figure 16.** Mosaic of LROC images M110601418L/R and M125936995L/R centered near 151.7°E, 4.1°S. The crater is at the center of a region of colder rock-free regolith temperatures termed "cold spots" shown in Figure 9. Although the relatively bright surface of the crater is typical of fresh craters, the continuous, layered nature of the ejecta is associated with craters with the colder surfaces beyond the continuous deposits.

### 4.4. Variations in Surface Unit Properties

[53] As has been anticipated, the presence of rocks is highly correlated with regions of increased brightness temperatures [e.g., *Mendell and Low*, 1974; *Urquhart and Jakosky*, 1997]. However, there are a number of locations where this correlation breaks down. There are variations in regolith temperatures that are apparently independent of the presence of rocks. This is best illustrated by comparing the temperatures of typical maria and highlands surfaces with dark mantled deposits and the cold spots. All of these surfaces typically have <0.5% rock concentration values, which is only sufficient to raise Diviner Channel 8 (100–200 $\mu$m) brightness temperatures by ~0.5 K. Both dark mantled deposits and cold spots show temperature reductions greater than this. Without the presence of rocks, the lower nighttime temperatures associated with dark mantled deposits and cold spots must be due to the physical properties of the regolith fines.

[54] ***Cold Spots.*** Dark mantled deposits are hypothesized to be composed of pyroclastic materials that are commonly composed of uniformly small particle sizes, which may account for their slightly lower rock-free regolith temperatures relative to typical lunar regolith fines. The 5–10 K lower temperatures present at the cold spots surrounding fresh craters is more difficult to explain. Typical lunar regolith fines are highly insulating, but there must be a process present related to the formation of these craters that creates a surface with a significantly lower thermal inertia.

[55] These cold surfaces (as well as the slightly cooler areas of Aristarchus Plateau) were noticed by *Mendell and Low* [1975] using Apollo 17 Infrared Scanning Radiometer data near Bessarion B. In this region, near 319E, 18N, temperatures were found to be as low as 88K. *Mendell and Low* [1975] did not identify the craters associated with these features and noted that there were no features in the photographic data associated with the cold surfaces themselves.

[56] Typical lunar surfaces have diurnal temperatures consistent with layering with an increased packing of materials at greater depths [*Keihm et al.*, 1973]. This leads to a slowing of surface cooling later in the lunar night due to the delayed influence of the higher thermal inertia materials present at a depth of a few centimeters. The colder regolith surfaces also show a temperature trend consistent with the presence of a packed layer at depth but are consistently colder than adjacent mare or highlands surfaces throughout the lunar night. This indicates that these surfaces have a lower thermal inertia at the surface than typical lunar regolith fines.

[57] The cold spots are related to young impact craters <2 km in diameter. Apollo, Clementine, and LROC images do not show any distinguishing albedo or morphology associated with the cold spots. Clementine multispectral data also do not display any distinguishing characteristics. High resolution LROC images do display unique characteristics, however. Most of the craters associated with cold spots have a relatively unique ejecta pattern within ~10 crater radii of the center (Figure 16). These surfaces have a radial, layered, and streaming pattern with distinct edges. Topographic features appear to have some control over the radial pattern that also displays some sinuosity. The abrupt edges and topographic influence indicate that this material was not emplaced ballistically and was likely due to a fluid-like density current. The actual cold regolith temperatures occur outside this region where radial streaks are still present, but the continuous layered pattern is absent. This may be due to the presence of rocks closer to the crater that would influence the derived regolith temperatures.

[58] The cold spots appear to be associated with young craters of unique morphological properties but are otherwise not unique with regards to the crater size, or terrain. The possibility that density currents were present to form these deposits suggests the presence of gasses, which is surprising for an airless planet with a volatile-poor regolith. However, it may be possible to deliver the volatiles necessary to produce density currents via an ice-rich impactor. A ~1.5 km diameter crater on the Moon can be produced by a ~50 m diameter comet [*Melosh*, 1989]. Assuming a composition of primarily ice, which is all converted into gas, this will produce ~0.65 $km^3$ of gas at standard temperature and pressure. A cometary impact at the lunar surface should produce gas volumes orders of magnitude larger, with higher temperatures and lower pressures. Such conditions should still be capable of producing density currents.

[59] Although detailed modeling of these impacts is beyond the scope of this work, it appears that recent cometary impacts are a plausible formation mechanism for these unique features. It is not clear, however, why the surrounding regolith is more highly insulating than typical lunar surfaces, though the presence of gas could perhaps be related to the formation of more delicately packed regolith

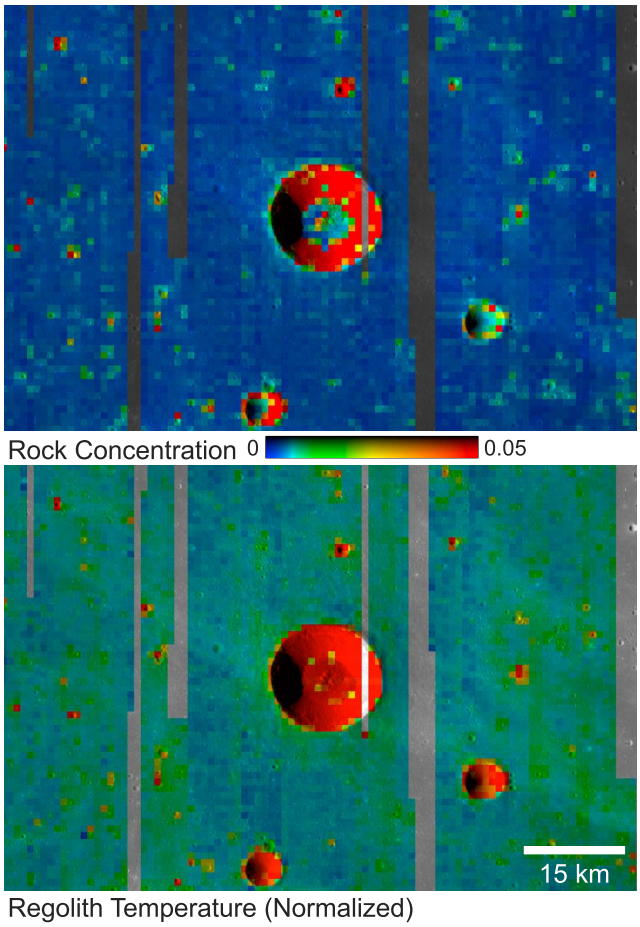


**Figure 17.** (top) Rock concentration and (bottom) regolith temperature images of Marius-A. The images are centered near 313.9°E, 12.6°N and the LROC WAC global mosaic is used for shading. The floor of the crater is relatively rock-free, but still contains uniformly elevated rock-free regolith temperatures. The radiative contribution from the walls of the crater is likely contributing to the higher temperatures rather than intrinsic thermophysical properties of the floor materials.

particles. There are other possible interpretations for the production of some of the morphological properties, however, such as ballistic erosion and sedimentation [*Oberbeck*, 1975]. Clearly, a more detailed and focused investigation of these morphologically and thermophysically unique craters is necessary.

#### 4.4.1. Crater Regolith Properties

[60] There is a clear correlation between regolith temperature and rock concentration values. It is not likely that this is a result of incorrect assumptions in the algorithm described here because large variations in regolith temperature due to factors such as variable local times, latitudes, or local slopes appear largely independent of the rock concentration determinations. This correlation is probably due to a combination of 3 factors; 1) smaller rocks are likely to be present that will remain somewhat warmer than regolith fines throughout the lunar night; 2) buried rocks are likely to be present that would elevate the temperature of the nighttime regolith; and 3) the presence of exposed rocks will radiatively heat the surrounding regolith. This correlation between regolith temperatures and rock concentration values appears to break down within craters. The floors of craters typically have lower rock concentrations than the crater walls and can be similar to the surrounding plains, with concentrations <0.01. By contrast, the floors of these craters have elevated regolith temperatures, typically ~15 K warmer than the surrounding plains (Figures 17 and 18). It is not clear if this patter persists for smaller craters (<3 km in diameter) as the floors are not clearly resolved at the 32 pixels per degree sampling.

[61] Similar to the cold regions, it appears that this is a case where regolith fines temperatures are decoupled from the presence of large blocks visible in high resolution images. There are several possible causes for the relative warmth of these surfaces despite the apparent absence of blocks. In the example shown in Figure 17, the crater Marius A has a diameter of 15 km and a depth of 5 km. From the center point of the crater, the rim of the crater is about 35 degrees above the level horizon. The walls will provide a substantial component of radiant energy to the floor of the crater that will keep the surface warmer than the surrounding plains, which are fully exposed to space. This effect is likely contributing to increased regolith temperatures in other regions, such as rilles. However, the elevated rock concentrations in these regions are not a result of this effect.

[62] There is also the possibility that the crater floor consists of a block size distribution that is largely devoid of blocks >1 m in diameter and is composed of coarser or more densely packed particles than typical lunar regolith. This would register as warmer regolith fines temperatures with relatively low rock concentrations. Although this is plausible, it is not clear what process would result in such a distribution of particle sizes on crater floors, especially because larger block sizes are expected to persist on the lunar surface longer than smaller blocks [e.g., *Hörz et al.*, 1975]. The higher temperatures can be explained by the extra radiance provided by the crater walls without invoking any additional

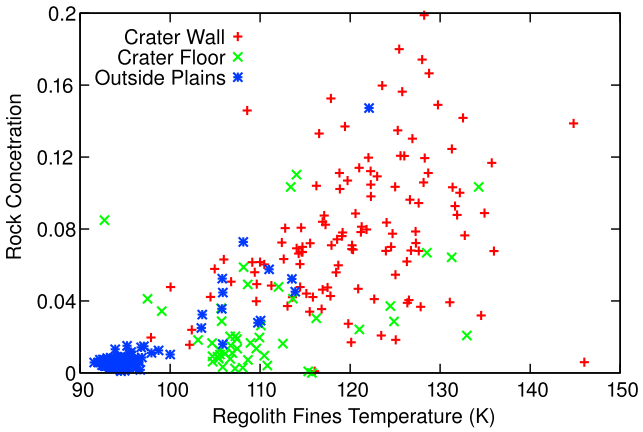


**Figure 18.** Rock concentration values versus rock-free regolith temperatures for the wall, floor, and outside plains of Marius-A shown in Figure 15.

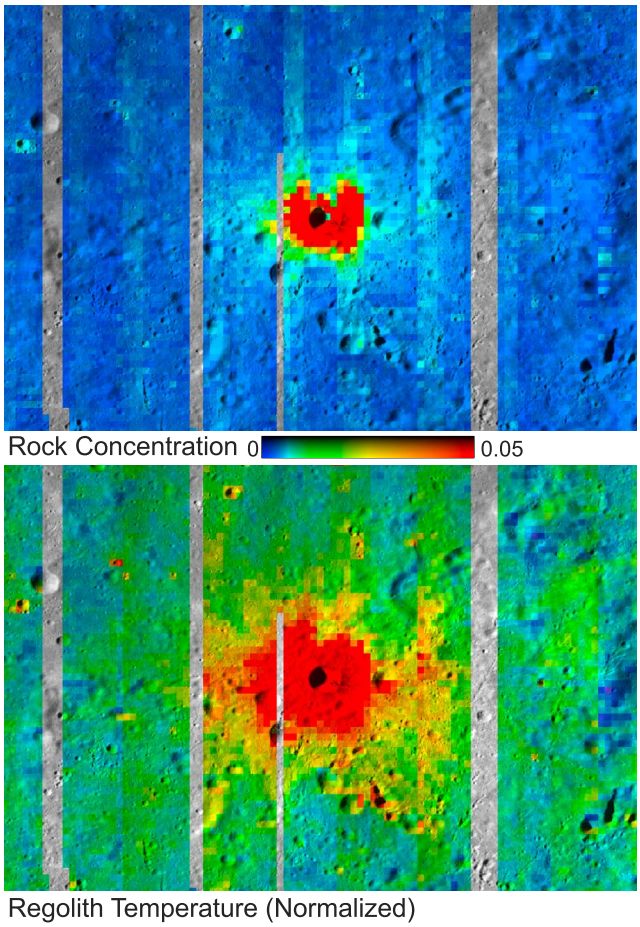


**Figure 19.** (top) Rock concentration and (bottom) regolith temperature images of Hell-Q. The images are centered near 355.5°E, 33.0°S and the LROC WAC global mosaic is used for shading. Regions of significantly elevated regolith temperatures extend to regions of only slightly elevated rock concentrations.

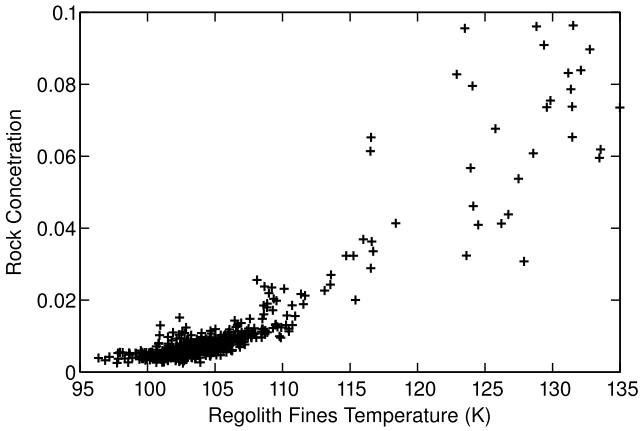


**Figure 20.** Rock concentration values versus rock-free regolith temperatures for the Hell-Q and its immediate surroundings shown in Figure 15.

complexity. This further illustrates that the rock concentration algorithm is indeed sensitive to the anisothermality from the presence of rocks over a mixed surface rather than simply translating warmer nighttime temperatures into elevated rock concentration values.

[63] By contrast, elevated rock concentrations are present over extended level surfaces outside of some young craters. For example, Hell-Q, a 3.8 km diameter crater centered near 355.5E, 33S is surrounded by a region of elevated regolith temperature that extends beyond the region of elevated rock concentrations (Figure 19). The elevated regolith temperatures do contain elevated rock concentrations, but are <0.015 despite regolith temperatures 10–15 K above that of the surrounding plains (Figure 20).

[64] Ejecta block sizes decrease with increasing distance from the crater [*Hörz et al.*, 1983; *Melosh*, 1989]. In the case of young craters, the original ejecta block distribution may be preserved as well as the clast size distribution as a function of distance from the crater. Hell-Q has elevated rock concentrations within 1–2 crater radii from the rim and elevated regolith temperatures within 4–5 crater radii. This separation of regolith and rock concentration properties likely represents a change in the surface particle size distributions. Although the more distal crater ejecta are largely free of larger blocks that would be detected by the rock abundance algorithm (or in LROC images), particles that are coarser or more densely packed than typical lunar regolith must be present. The separation of rock concentrations and regolith fines temperatures allows for the retrieval of some minimal clast size distribution information.

[65] That these warm regolith temperatures only occur around immature craters is consistent with previous work that predicts much longer survival times for larger rocks. In this environment, 0.1 and 1 m diameter rocks were found to have median survival times of ~10 and 100 million years respectively [*Hörz et al.*, 1975]. This effect may explain why elevated rock abundances persist near older craters even though the extended regions of elevated regolith temperatures do not.

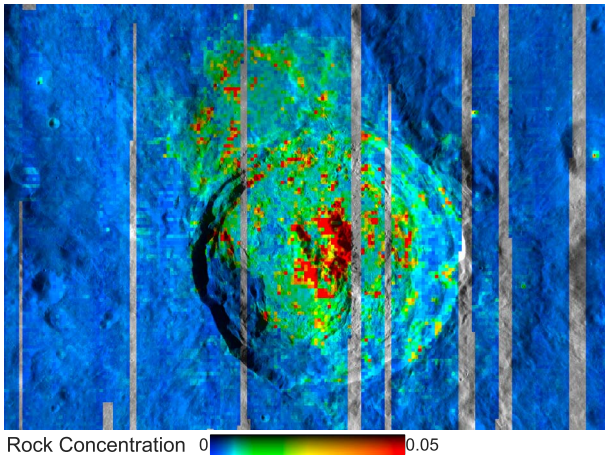


**Figure 21.** Rock concentration values near King Crater. The image is centered near 120.5°E, 5.0°N and the LROC WAC global mosaic is used for shading. Slightly elevated rock concentrations are associated with the impact melt northwest of the crater rim, but are typically restricted to steep slopes or recent small impact craters.

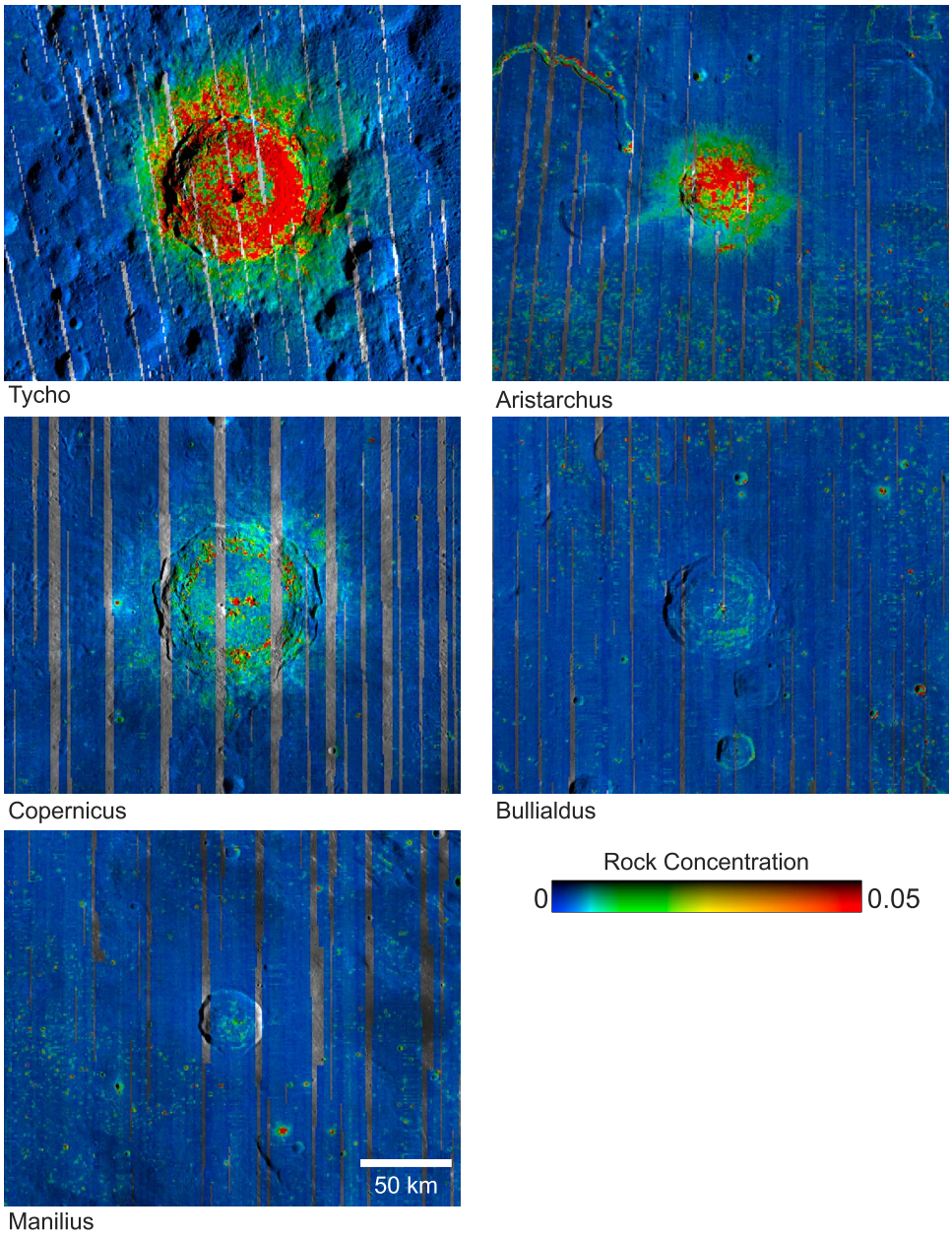


**Figure 22.** Rock concentration values with the LROC WAC global mosaic used for shading. Rock concentrations are progressively diminished with increasing age. Craters shown (from youngest to oldest; *Neukum and Koenig* [1976]) are Tycho (Copernican period), Arstarchus (Copernican), Copernicus (Copernican), Bullialdus (Eratosthenian), and Manilius (Eratosthenian).

#### 4.4.2. Impact Melts

[66] The rock concentration distributions near craters and rilles illustrates that exposure of rocks requires mass wasting to keep the surface free of mantling regolith. Relatively level surfaces are commonly free of rocks with the exception of very young craters such as the Hell-Q example described above. Impact melts, such as those exposed immediately northwest of King Crater, also illustrate this property. King Crater is a Copernican Age crater dated to ~1 Ga [*Ashley et al.*, 2011]. The central peak, crater walls, and the perimeter of the impact melt region have elevated rock concentrations. The crater ejecta has only slightly elevated rock concentrations within about half a crater radius from the rim.

[67] The impact melt region clearly contains rocky surfaces, but these are limited to steeper and rough terrains and areas adjacent to these terrains or within impact craters on the melt region (Figure 21). Relatively featureless and level surfaces have been mantled by an insulating regolith cover. This cover is likely to be quite thin as small impacts on these surfaces expose rocks that are clearly visible in LROC images. *Mendell* [1976] also noticed the lack of elevated temperatures over impact melts in Copernicus Crater. It is possible that mass wasting of fine particulate material from crater walls mantles the floor or that somehow impact melts have mechanical properties that result in a more rapid development of regolith cover [*Mendell*, 1976]. In the case

of King Crater, the melt is extensive enough and external to the crater so that mantling of the material through mass wasting from adjacent steep slopes is not possible. Although some impact melt surfaces may be relatively young and likely started without a regolith cover, the development of regolith over these surfaces over time appears to be similar to that of crater ejecta deposits and rock concentrations are typically less than a few percent.

#### 4.4.3. Crater Ages and Regolith Thickness

[68] As has been noted previously, rocks exposed at the surface in the lunar environment are degraded over time, primarily by micrometeorite impacts [*Thompson et al.*, 1974; *Mendell*, 1976]. As a result, only younger craters show elevated rock concentrations. For example, a trend of decreasing rock concentration with increasing age was noticed between Aristarchus, Kepler, and Copernicus Craters by *Mendell* [1976].

[69] Large young craters, such as Tycho, Giordano Bruno, and Aristarchus, have continuous areas of elevated rock concentrations that include the crater interior, rim and proximal ejecta. There is a clear contrast in both abundance and spatial pattern of the surfaces bearing elevated rock concentrations with older Copernican craters, such as Copernicus and Kepler. These older Copernican aged craters have limited areas of highly elevated rock concentrations that are present on steep slopes. Elevated rock concentrations (and regolith temperatures) are present on the floor and proximal ejecta blanket, but these values are typically less than ~2%. This trend continues with further subdued rock concentrations and extents in Eratosthenian aged craters that have only slightly elevated rock concentrations and no apparent increased rock concentrations immediately outside the crater rim. A general trend between crater age and rock abundance is clear from comparison of rock concentration values between craters of a range of ages (Figure 22) [*Neukum and Koenig*, 1976]. Although it is likely that target rock type and crater size influence the exposure of rocks at the lunar surface, it is apparent that the relative age of crater formation can be quickly estimated by the extent and values of increased rock concentrations associated with the crater. This requires that the crater is large enough to excavate material beneath the local fine particulate regolith. This is typically the case for craters greater than several 10s of km in diameter.

[70] The association of crater size with excavation depth allows for the estimation of regolith thickness. A full assessment of regolith thickness from the association of rock concentrations with crater diameter is beyond the scope of this work. However, it is apparent that numerous small craters excavate rocks within the younger Mare surfaces. This pattern is absent from both highlands and within the extended ejecta blankets of craters with radar dark "haloes."

[71] There are exceptions to this pattern. Dark mantled deposits, for example, do not contain elevated rock concentrations associated with small craters. This may not represent regolith thickness, however, as these deposits are likely to be pyroclastic in nature and may not be of sufficient strength to survive ejection and subsequent impact in a cratering event. In addition, it is not uncommon for small (<1 km diameter) younger craters in the lunar highlands to display elevated rock concentrations. This implies that the lunar regolith thickness may be quite variable within the highlands and rocky materials may be close to the surface in isolated locations.

## 5. Conclusions

[72] LRO Diviner radiometer data have been used to produce rock concentration and regolith temperature maps within 60°N/S latitude. Although the data and model used here are relatively simple and necessarily require simplifying assumptions, there are clear correlations with blocks visible in LROC images. There are also correlations with radar CPR data sets. The Diviner rock concentration and regolith temperature data discussed here are publicly available at the Planetary Data System.

[73] The derivation of rock abundance is largely driven by anisothermality between spectral channels. Residual heating on western facing slopes after sunset, for example, will display higher regolith fines temperatures, but derived rock concentration values are largely unaffected. In addition, crater floors, cold spots, dark mantled deposits, and distal ejecta from young craters show trends in regolith temperature independent of the presence of rocks. The crater floors are likely warmed by downwelling radiance from adjacent crater walls. However, in the other cases, regolith properties appear to have qualities different from typical lunar highlands and maria regolith. There is a clear contrast between isothermal and anisothermal surfaces and the Diviner multispectral data have been used to distinguish between these surfaces.

[74] The extent and absolute value of rock concentrations is correlated with crater age. Rocky surfaces are only preserved on the youngest surfaces or where steep slopes occur and mass wasting prevents mantling with fines. The presence of rocky surfaces excavated by young impacts allows for the estimation of minimum regolith thickness from the size of the impact. A first order assessment shows that maria surfaces typically have a thin regolith cover and many crater ejecta and the lunar highlands have a thicker regolith, as has been previously established. However, the excavation of rocky surfaces by small craters in the lunar highlands implies that this thick regolith is not uniform.

[75] What we have described here is only an initial description and assessment of the rock concentration and regolith fines temperature data sets. There appears to be a great deal of potentially useful information present in these data and further validation, comparisons with other data sets, and focused studies are planned.

[76] **Acknowledgments.** We would like to thank the spacecraft and Diviner operations teams at Goddard Space Flight Center, Jet Propulsion Laboratory, and UCLA for their support. Comments from Sylvain Piqueux and an anonymous reviewer were quite constructive and we hope that the manuscript has been significantly improved as a result of our efforts to address them. Support to J.L.B. for this work was provided by NASA grant NNX08AT73G under the Lunar Reconnaissance Orbiter Participating Scientist Program.

## References

Ashley, J. W., et al. (2011), Geologic mapping of the King Crater region with an emphasis on melt pond anatomy: Evidence for subsurface drainage on the Moon, *Proc. Lunar Planet. Sci. Conf.*, *42*, 2437.

Bandfield, J. L. (2009), Effects of surface roughness and graybody emissivity on Martian thermal infrared spectra, *Icarus*, *202*, 414–428, doi:10.1016/j.icarus.2009.03.031.

Bandfield, J. L., and C. S. Edwards (2008), Derivation of Martian surface slope characteristics from directional thermal infrared radiometry, *Icarus*, *193*, 139–157, doi:10.1016/j.icarus.2007.08.028.

Campbell, B. A., B. R. Hawke, and T. W. Thompson (1997), Regolith composition and structure in the lunar maria: Results of long-wavelength radar studies, *J. Geophys. Res.*, *102*, 19,307–19,320, doi:10.1029/97JE00858.

Campbell, B. A., D. B. Campbell, J. L. Margot, R. R. Ghent, M. Nolan, J. Chandler, L. M. Carter, and N. J. S. Stacy (2007), Focused 70-cm wavelength radar mapping of the Moon, *IEEE Trans. Geosci. Remote Sens.*, *45*, 4032–4042, doi:10.1109/TGRS.2007.906582.

Campbell, B. A., L. M. Carter, D. B. Campbell, M. Nolan, J. Chandler, R. R. Ghent, B. Ray Hawke, R. F. Anderson, and K. Wells (2010), Earth-based 12.6-cm wavelength radar mapping of the Moon: New views of impact melt distribution and mare physical properties, *Icarus*, *208*, 565–573, doi:10.1016/j.icarus.2010.03.011.

Christensen, P. R. (1986), The spatial distribution of rocks on Mars, *Icarus*, *68*, 217–238, doi:10.1016/0019-1035(86)90020-5.

Cintala, M. J., and K. M. McBride (1995), Block distributions on the lunar surface: A comparison between measurements obtained from surface and orbital photography, *NASA Tech. Memo. 104804*.

Colwell, J. E., and B. M. Jakosky (2002), Effects of topography on thermal infrared spectra of planetary surfaces, *J. Geophys. Res.*, *107*(E11), 5106, doi:10.1029/2001JE001829.

Gaddis, L. R., C. M. Pieters, and B. R. Hawke (1985), Remote sensing of lunar pyroclastic mantling deposits, *Icarus*, *61*, 461–489, doi:10.1016/0019-1035(85)90136-8.

Ghent, R. R., D. W. Leverington, B. A. Campbell, B. R. Hawke, and D. B. Campbell (2005), Earth-based observations of radar-dark crater haloes on the Moon: Implications for regolith properties, *J. Geophys. Res.*, *110*, E02005, doi:10.1029/2004JE002366.

Ghent, R. R., B. A. Campbell, B. R. Hawke, and D. B. Campbell (2008), Earth-based radar data reveal extended deposits of the Moon's Orientale basin, *Geology*, *36*, 343–346, doi:10.1130/G24325A.1.

Heiken, G. H., D. T. Vaniman, and B. M. French (1991), *Lunar Sourcebook: A User's Guide to the Moon. Research Supported by NASA*, 753 pp., Cambridge Univ. Press, Cambridge, U. K.

Helfenstein, P., and J. Veverka (1987), Photometric properties of lunar terrains derived from Hapke's equation, *Icarus*, *72*, 342–357, doi:10.1016/0019-1035(87)90179-5.

Horai, K.-I., and G. Simmons (1972), Thermal property measurements on lunar material returned by Apollo 11 and 12 missions, *Progress Astronaut. Aeronaut.*, *28*, 243–267.

Hörz, F., E. Schneider, D. E. Gault, J. B. Hartung, and D. E. Brownlee (1975), Catastrophic rupture of lunar rocks: A Monte Carlo simulation, *Moon*, *13*, 235–258, doi:10.1007/BF00567517.

Hörz, F., R. Ostertag, and D. A. Rainey (1983), Bunte breccia of the Ries: Continuous deposits of large impact craters, *Rev. Geophys. Space Phys.*, *21*, 1667–1725, doi:10.1029/RG021i008p01667.

Keihm, S. J., K. Pieters, M. G. Langseth, and J. L. Chute Jr. (1973), Apollo 15 measurements of lunar surface brightness temperatures thermal conductivity of the upper 1 1/2 meters of regolith, *Earth Planet. Sci. Lett.*, *19*, 337–351, doi:10.1016/0012-821X(73)90084-8.

Melosh, H. J. (1989), *Impact Cratering: A Geologic Process*, *Oxford Monogr. Geol. Geophys.*, vol. 11, 253 pp., Oxford Univ. Press, New York.

Mendell, W. W. (1976), Degradation of large, period II lunar craters, *Proc. Lunar Planet. Sci. Conf.*, *7*, 2705–2716.

Mendell, W. W., and F. J. Low (1974), Preliminary results of the Apollo 17 infrared scanning radiometer, *Moon*, *9*, 97–103, doi:10.1007/BF00565396.

Mendell, W. W., and F. J. Low (1975), Infrared orbital mapping of lunar features, *Proc. Lunar Planet. Sci. Conf.*, *6*, 2711–2719.

Neukum, G., and B. Koenig (1976), Dating of individual lunar craters, *Proc. Lunar Planet. Sci. Conf.*, *7*, 2867–2881.

Nowicki, S. A., and P. R. Christensen (2007), Rock abundance on Mars from the Thermal Emission Spectrometer, *J. Geophys. Res.*, *112*, E05007, doi:10.1029/2006JE002798.

Nozette, S., et al. (2010), The Lunar Reconnaissance Orbiter Miniature Radio Frequency (Mini-RF) technology demonstration, *Space Sci. Rev.*, *150*, 285–302, doi:10.1007/s11214-009-9607-5.

Oberbeck, V. R. (1975), The role of ballistic erosion and sedimentation in lunar stratigraphy, *Rev. Geophys.*, *13*, 337–362, doi:10.1029/RG013i002p00337.

Paige, D. A., et al. (2010), The Lunar Reconnaissance Orbiter Diviner Lunar Radiometer experiment, *Space Sci. Rev.*, *150*, 125–160, doi:10.1007/s11214-009-9529-2.

Price, S. D., D. Mizuno, and T. L. Murdock (2003), Thermal profiles of the eclipsed Moon, *Adv. Space Res.*, *31*, 2299–2304, doi:10.1016/S0273-1177(03)00531-3.

Robinson, M. S., et al. (2010), Lunar Reconnaissance Orbiter Camera (LROC) instrument overview, *Space Sci. Rev.*, *150*, 81–124, doi:10.1007/s11214-010-9634-2.

Roelof, E. C. (1968), Thermal behavior of rocks on the lunar surface, *Icarus*, *8*, 138–159, doi:10.1016/0019-1035(68)90069-9.

Shorthill, R. W. (1970), Infrared Moon: A review, *J. Spacecraft Rockets*, *7*, 385–397, doi:10.2514/3.29952.

Thompson, T. W., H. Masursky, R. W. Shorthill, G. L. Tyler, and S. H. Zisk (1974), A comparison of infrared, radar, and geologic mapping of lunar craters, *Moon*, *10*, 87–117, doi:10.1007/BF00562019.

Tooley, C. R., M. B. Houghton, R. S. Saylor, C. Peddie, D. F. Everett, C. L. Baker, and K. N. Safdie (2010), Lunar Reconnaissance Orbiter Mission and spacecraft design, *Space Sci. Rev.*, *150*, 23–62, doi:10.1007/s11214-009-9624-4.

Urquhart, M. L., and B. M. Jakosky (1997), Lunar thermal emission and remote determination of surface properties, *J. Geophys. Res.*, *102*, 10,959–10,969, doi:10.1029/97JE00224.

Vasavada, A. R., D. A. Paige, and S. E. Wood (1999), Near-surface temperatures on Mercury and the Moon and the stability of polar ice deposits, *Icarus*, *141*, 179–193, doi:10.1006/icar.1999.6175.

J. L. Bandfield, Johnson Hall 070, Box 351310, University of Washington, Seattle, WA 98195-1310, USA. (joshband@u.washington.edu)

R. R. Ghent, Department of Geology, University of Toronto, Earth Sciences Centre, 22 Russell St., Toronto, ON M5S 3B1, Canada.

S. J. Lawrence and M. S. Robinson, School of Earth and Space Exploration, Arizona State University, Tempe, AZ 85251, USA.

D. A. Paige, Earth and Space Sciences, UCLA, PO Box 951567, Los Angeles, CA 90095-1567, USA.

A. R. Vasavada, Jet Propulsion Laboratory, California Institute of Technology, M.S. 321-220, 4800 Oak Grove Dr., Pasadena, CA 91109, USA.